

# A Bare-Earth Extraction Algorithm Based on Graph Cut Segmentation for Electro-Optically-Derived Point Clouds

Eric Hardin

ehardin@ara.com

Applied Research Associates, Inc.

March 11, 2019

## Abstract

This paper introduces a new bare-earth algorithm based on Markov Random Field image segmentation. Many bare-earth algorithms exist that were developed for LiDAR. However, a new algorithm was needed to extract bare-earth from point clouds produced by stereo-matching multi-view satellite imagery (called electro-optic (EO) point clouds). EO point clouds have characteristics that pose challenges distinct from LiDAR such as substantially greater noise levels and missing data due to object occlusion. Despite these challenges, the algorithm accurately extracts bare-earth from EO point clouds. Additionally, the algorithm is robust to sensor type, which was demonstrated by applying the algorithm to LiDAR surveys collected with different sensors. The algorithm is shown to be robust to different levels of urban development and terrain variability and achieves a 94% accuracy on average when compared to manually classified point clouds.

## 1 Introduction

Reconstruction of urban areas in an automated fashion is important for visualization, simulation, and training (among other applications) within domains such as urban planning, humanitarian operations, and military training [1]. Different problem domains require different levels of accuracy and

detail. This work is part of a broader effort to create accurate, photo-realistic synthetic environments of real urban areas from point cloud data.

The focus of this paper is bare-earth extraction. Bare-earth is the first feature extracted in our pipeline because it is often the single largest, continuous feature in the scene. Further, bare-earth is used to extract other features, e.g., it provides a surface from which to measure vegetation and building heights.

Our work necessitated a new bare-earth algorithm. bare-earth extraction has been a research problem since the advent of LiDAR mapping (approximately 20 years ago), and many effective approaches have been developed [2]. However, these algorithms were developed for airborne LiDAR, whereas our aim is to extract bare-earth from electro-optically derived (EO) point clouds. Furthermore, although EO point clouds are our focus, our work involves multiple data sources; therefore it is highly desirable that our bare-earth algorithm can extract accurate bare-earth from various types of point clouds, i.e., EO as well as direct mode and Geiger mode LiDAR.

Our aim is to develop a bare earth algorithm that operates on EO point clouds because EO point clouds can often be the preferred, if not the only, source of high-resolution terrain data. EO point clouds are produced by stereo-matching multi-view satellite imagery, and due to the passive nature of imaging they are also called passive point clouds. Performing large-scale photogrammetry from satellite imagery has become more tractable due to advances in 3D photogrammetry algorithms and improvements in computing resources. Furthermore, EO point clouds have the advantage that imaging can occur in near-real time anywhere globally (including those areas where flying an aircraft is not possible).

EO point clouds have characteristics that pose challenges for feature extraction. Unlike LiDAR, EO point clouds:

- often have much greater noise levels (often 50 cm vertically in contrast to 0.12-0.15 cm for LiDAR)
- regularly have large areas of missing data where buildings and other large objects block the vantage point of a satellite
- rarely capture ground points under dense canopies or between closely spaced buildings, in contrast to LiDAR that penetrates to the earth through small openings to provide a more uniform distribution of bare-earth points

Popular bare-earth algorithms were developed for LiDAR [2] and tend to struggle with EO point clouds. We evaluated two algorithms for extracting bare-earth from EO point clouds, which represent two of the leading approaches to bare-earth extraction. The algorithms were an implementation of the Hierarchical Robust Interpolation algorithm [3] and the LasGround tool as part of LasTools [4]. Neither algorithm produced satisfactory bare-earth when applied to an EO point cloud.

Therefore, we developed a new algorithm based on [5] and [6]. We chose an approach similar to [6] because they developed their algorithm to operate on stereo-matched aerial imagery, which is characteristically similar to EO point clouds derived from stereo-matched satellite imagery.

[6] treats terrain classification as a Hidden Markov Random Field (MRF), which is an approach that is particularly well suited for bare-earth extraction. MRF modeling is an inverse-problem approach that attempts to compute an unobservable (hidden) state of a system based on an observable manifestation of that underlying state. In the case of bare-earth extraction, an object’s terrain/off-terrain nature is hidden, but it results in the features observed in the elevation field, i.e., the Digital Surface Model (DSM). The Markov assumption is that local interactions are enough to determine the state on a larger set. Local interactions encode spatial continuity, which is advantageous especially for EO point clouds that are typically very noisy and contain data voids.

MRF for image segmentation and reconstruction was pioneered by Geman and Geman in 1984 [7]. Due in part to its robustness to noise and missing data, it has since been applied to, e.g., robot navigation [8, 9], segmentation of features in medical images [10], and classification of satellite imagery [11, 12].

This paper describes our MRF formulation. We show that the algorithm is capable of accurately segmenting terrain from off-terrain features in an EO point cloud. Furthermore, we demonstrate that the algorithm is robust to sensor type by extracting bare-earth from direct-mode and Geiger-mode LiDAR data. As a result, we show that the MRF approach is a valuable bare-earth extraction technique – not only for its ability to extract earth from EO point clouds, but also for its applicability to various kinds of point clouds. We continue by reporting the algorithm performance and, finally, we discuss some of the shortcomings of the algorithm and future work.

## 2 Method

### 2.1 Markov Random Fields

Surveying methods such as EO and LiDAR produce an unlabeled DSM. We pose that the features in the DSM are the observable result of whether those features are terrain or off-terrain objects (which we ultimately desire to know). This exemplifies the crux of a Hidden Markov Model, which assumes that the studied system exhibits an observable outcome due to an unobservable, underlying state. Therefore, to label the objects in a scene as terrain or off-terrain, we look for the labeling that maximizes the likelihood of the observed DSM. It is our task to devise a relationship between the state of the system and the observable result.

Given a model that relates the DSM to the label map, the number of possible label maps makes the problem combinatorial and solution via rote enumeration intractable. However, there are some common measures to simplify the problem.

First, the Hammersley-Clifford theorem says that under certain conditions local interactions are enough to determine a random variable on a larger set. That is, the probability of observing the actual DSM given the global label map can be factored into the compound probability of the observation in each local neighborhood (called a clique) [13]:

$$P(L) = \prod_C P(L_C) \quad (1)$$

where  $P(L)$  is the probability of observing a global labeling  $L$ , and  $P(L_C)$  is the probability of observing the labeling within a clique,  $C$ .

Second, we can treat the labeling problem as an energy minimization problem by expressing the probability as a potential [13]:

$$P(L_C) = \frac{1}{Z} e^{-\beta E_C(x)} \quad (2)$$

where  $E_C$  is the potential function of the state  $x$ ,  $Z$  is a normalization constant, and  $\beta$  is a free parameter. Finding the state that minimizes the energy is equivalent to finding the most likely label map.

## 2.2 Energy Formulation

With the MRF and energy minimization framework in place, our task is to formulate energy potentials that, when minimized, yield terrain/off-terrain labels that are consistent with human interpretation or ground truth. MRF energies come from two sources, which are data energy and clique potential. Data energy typically grows with the difference between an observation at a pixel and the class mean (e.g., a pixel’s data energy will be large if it is labeled terrain but its elevation is considerably greater than neighboring terrain pixels). Clique potential is typically incurred when the class of a pixel disagrees with those in its clique (e.g., a pixel’s clique potential will be large if it is labeled terrain but it is surrounded by off-terrain pixels).

The total energy is

$$E_{tot} = \alpha E_{data} + (1 - \alpha) E_{clique} \quad (3)$$

where  $E_{data}$  and  $E_{clique}$  are the data energy and clique potential, and  $\alpha$  is a tunable parameter between zero and unity. Larger values of  $\alpha$  will fit the data more closely whereas smaller values of  $\alpha$  will promote spatial continuity of segmented features.

### 2.2.1 Data Energy

Following [6], our data energy is

$$E_{terrain} = \begin{cases} 0 & z_{dsm} - z_{dtm} \leq \delta_0 \\ 1 - \exp \left\{ -c \left( \frac{(z_{dsm} - z_{dtm}) - \delta_0}{\delta_0} \right)^2 \right\} & z_{dsm} - z_{dtm} > \delta_0 \end{cases} \quad (4)$$

$$E_{off-terrain} = \begin{cases} 1 - \exp \left\{ -c \left( \frac{(z_{dsm} - z_{dtm}) - \delta_0}{\delta_0} \right)^2 \right\} & z_{dsm} - z_{dtm} \leq \delta_0 \\ 0 & z_{dsm} - z_{dtm} > \delta_0 \end{cases} \quad (5)$$

where  $E_{terrain}$  and  $E_{off-terrain}$  are the data energies incurred by a pixel that assumes the terrain or off-terrain classification,  $z_{dsm}$  and  $z_{dtm}$  are the elevations of the DSM and DTM,  $\delta_0$  is the half-width of the Gaussian (which is a tunable parameter), and  $c = \ln 2$  is a constant. The parameter  $c$  was set so that the potential is at its half-maximum when the rest of the exponent equals one, which gives  $\delta_0$  an intuitive interpretation as the half-width measured in meters.

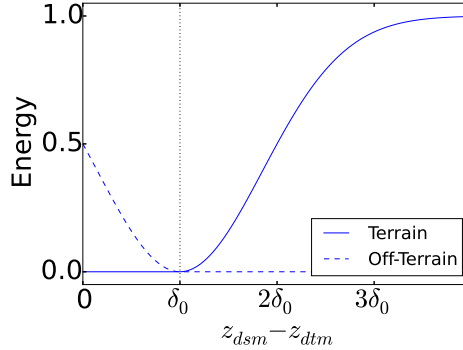


Figure 1: Data energy for pixels that have assumed the terrain and off-terrain classifications as a function of the detrended elevation. The detrended elevation is the state of our MRF system.

The state of the system in our MRF (Eq. 5) is the detrended elevation  $z_{dsm} - z_{dtm}$ . The data energy as a function of the detrended elevation is shown in Figure 1. This results in a nonlinearity in that the detrended elevation is computed from the DTM elevation, which is computed from the label map. We estimate the elevation of the DTM at the  $i^{th}$  pixel as the average elevation of terrain pixels within a set radius. The radius is an important parameter because setting the radius too large may smooth away salient terrain features, whereas setting the radius too small may fail to capture any terrain pixels (e.g., at the center of a large-footprint building).

In addition to the smoothing radius,  $\delta_0$  is also an important parameter. Useful starting values of  $\delta_0$  will be roughly half a building story (about 1.5 m) because the truncated Gaussian formulation encourages pixels to assume the terrain label if their elevation is within  $\delta_0$  of the local terrain elevation.

### 2.2.2 Clique Potential

Our clique potentials are constructed from truncated Gaussian potentials to yield trends similar to [6] (Figure 2). Sources of clique potential combine additively, i.e., Eq. 6-9 sum to equal  $E_{clique}$  in Eq. 3.

We model the interaction between pixels of different labels using truncated, zero-centered Gaussian potentials (Eqs. 8 and 9). Gaussian clique potentials arise from continuous fields with Gaussian distributed error [13].

The terrain is largely continuous (although exceptions exist such as retaining walls) and the residual once the elevation is detrended is approximated by a Gaussian distribution. We truncate the Gaussian to maintain the maximum potential for, e.g., a terrain pixel at a higher elevation than an off-terrain pixel. This represents the fact that the binary labels are not arbitrary in that terrain is always the lowest-elevation label.

We model the interaction between adjacent terrain pixels with a Gaussian well (Eqs. 8). Assuming the terrain is continuous, adjacent terrain pixels with similar elevation should not incur energy, whereas a significant difference in elevations suggests that the pixels belong to different classes. Adjacent off-terrain pixels do not incur clique potential (Eqs. 7) because adjacent off-terrain pixels can often be at different elevations (e.g., a multi-level building).

#### **Terrain-Terrain**

$$E = 1 - \exp \left\{ -c \left( \frac{\Delta z_{dsm}}{\delta_0} \right)^2 \right\} \quad (6)$$

#### **Building-Building**

$$E = 0 \quad (7)$$

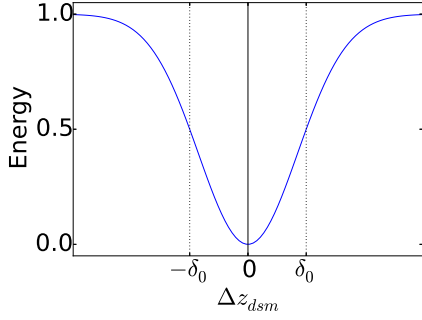
#### **Terrain-Building**

$$E = \begin{cases} \exp \left\{ -c \left( \frac{\Delta z_{dsm}}{\delta_0} \right)^2 \right\} & \Delta z_{dsm} \leq 0 \\ 1 & \Delta z_{dsm} > 0 \end{cases} \quad (8)$$

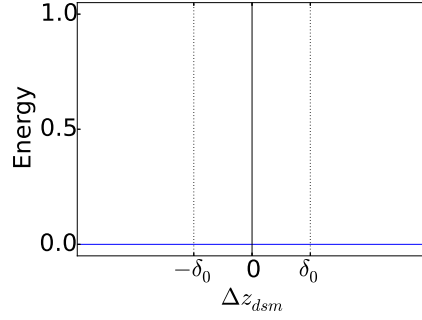
#### **Building-Terrain**

$$E = \begin{cases} 1 & \Delta z_{dsm} \leq 0 \\ \exp \left\{ -c \left( \frac{\Delta z_{dsm}}{\delta_0} \right)^2 \right\} & \Delta z_{dsm} > 0 \end{cases} \quad (9)$$

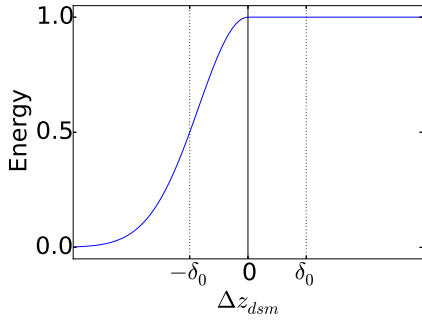
$\Delta z_{dsm}$  is the DSM elevation difference between a pixel and another in its clique.



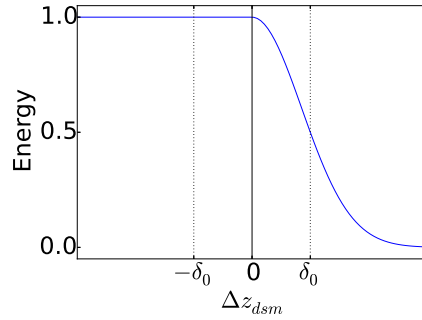
(a) Terrain/Terrain Potential



(b) Off-terrain/Off-terrain Potential



(c) Terrain/Off-Terrain Potential



(d) Off-Terrain/Terrain Potential

Figure 2: Clique potentials for each combination of pixel classification as a function of the elevation differences between the neighboring pixels. The clique potentials encode the assumption of spatial continuity in object classification. Furthermore, the clique potentials enforce that bare earth is always lower than non-earth objects.



## 2.3 Energy Minimization

Given the energy potentials in Eq. 4 through 9, we find the terrain/off-terrain classification by minimizing the energy. [6] minimizes the energy using simulated annealing ([5] used Iterative Conditional Modes). Simulated annealing is a stochastic energy minimization technique that is discussed in [7] in the context of image segmentation with MRF.

In contrast to simulated annealing, we minimize the energy using graph cuts (also referred to as min-cut/max-flow or s-t cuts). We chose to minimize the energy using graph cut segmentation since it is exact for binary labeling and efficiently solvable (in polynomial time), whereas simulated annealing is only exact at infinite time and usually requires long runtimes. We used the min-cut/max-flow algorithm developed by [14]. The authors of [6] did not have the advantage of the max-flow algorithm of [14] because it was published two years later.

In a graph theoretic picture, the image is represented as a directed graph with  $N + 2$  nodes where  $N$  is the number of pixels in the image. Each pixel has a corresponding node in the graph, and each of these nodes are connected to the other nodes in its clique. The two remaining nodes are the source (from which each pixel node connects) and the sink (to which each pixel node connects). Each connection has an associated affinity, which has an inverse interpretation of an MRF energy in that nodes with similar attributes have stronger affinities.

A min-cut computes the binary segmentation of an image by severing the minimum number of low-affinity connections until there is no longer a path connecting the source to the sink. Nodes that remain connected to the source assume one class (e.g., terrain) and nodes connected to the sink assume the other class (e.g., off-terrain).

While min-cuts are still a combinatorial approach, max-flow provides an equivalent, efficiently solvable approach. A max-flow algorithm computes the maximum steady-state flow from the source to the sink through the graph edges, where flow capacity is equal to affinity. The saturated edges are those that would be cut in a min-cut. The max-flow approach was first applied to binary image labeling by [15] in 1989.

Although graph cuts are exact, energy minimization is nonlinear due to the dependence of the data potential on the DTM and the dependence of the click potential on the pixel labels. For this reason, we applied graph cuts iteratively. The algorithm begins with an initial label map (which could be

Site	Sensor	Area (km <sup>2</sup> )	points (10 <sup>6</sup> )	Lat	Lon
I	EO	1	3.4	36.32552	43.18502
II	Direct Mode	0.375	2.2	28.58373	-81.18542
III	ALIRT	3	3.5	34.39186	68.82483
IV	BuckEye	1	1.5	36.34212	43.12259

Table 1: Study site details

random or a heuristic best guess). Given pixel labels, a DTM is interpolated. Subsequently, the data potential is computed and the pixel labels are used to update the clique potentials. Then, a graph cut is performed to yield new pixel labels. This is repeated until a stopping criterion is met. We chose to stop iterating when fewer than 0.05% of the pixels change their label during an iteration.

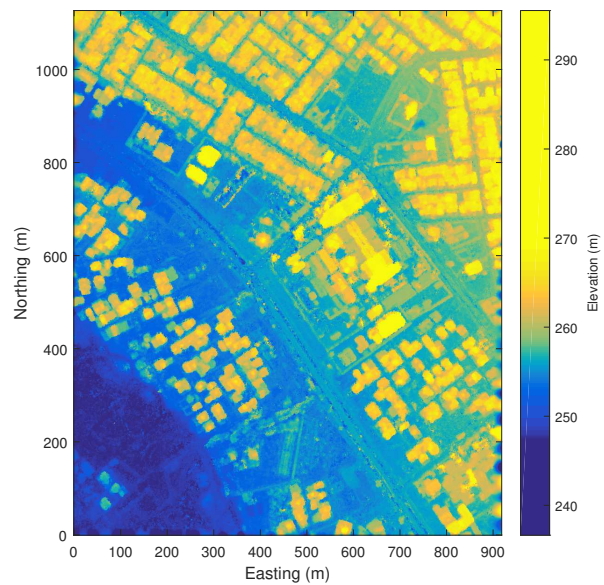
## 2.4 Datasets

We tested the algorithm with four datasets. The datasets were collected with different types of sensors and at locations that have different building and terrain characteristics. The four point clouds represent four common sensors used to generate high-resolution point clouds, which are EO, direct-mode aerial LiDAR, Buckeye LiDAR and ALIRT LiDAR. The scenes were chosen to test the algorithm against varying degrees of urban and rural, different architectural styles, and variability of terrains. 1 summarizes the study sites.

Site I is in Mosul Iraq. The point cloud is derived from Digital Globe WorldView-2 imagery. Figure 3 shows that the scene contains the Al-Salam Hospital and other multi-level structures. The terrain has a slight slope with a shelf where the land-use transitions from developed to agricultural. This point cloud has some occlusion near the largest buildings, and a prevalence of noise and outliers. These characteristics are typical of EO point clouds.

Site II is outside of Orlando, FL, USA. This point cloud was collected by a direct mode LiDAR system flown from a low-altitude, small aircraft. Figure 4 shows that the scene contains hip- and gable-roofed homes, and an elementary school. The area also has scattered trees and largely flat terrain (with the exception of storm water retention ponds).

Site III is in Mami Khel, Afghanistan, which is about 30 km southwest of Kabul. This point cloud was collected by MIT Lincoln Laboratory’s Airborne Ladar Imaging Research Testbed (ALIRT) system [16], which is a Geiger-

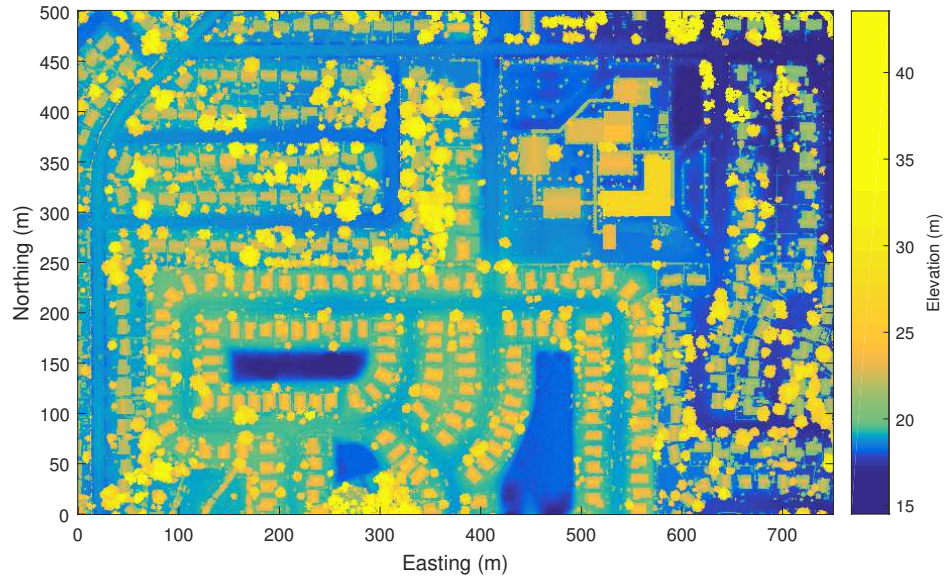


(a) DSM

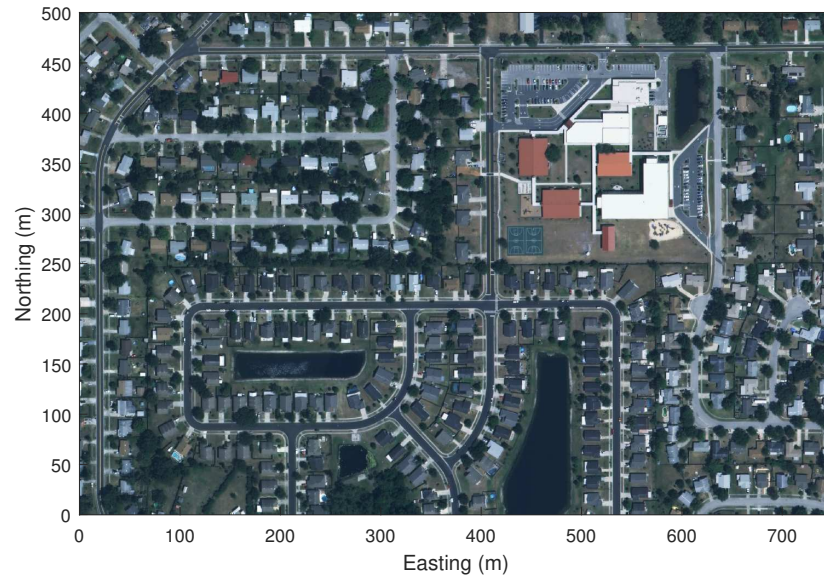


(b) Orthoimage

Figure 3: DSM from EO-derived point cloud and orthoimage of study area



(a) DSM



(b) Orthoimage

Figure 4: DSM from direct-mode LiDAR point cloud and orthoimage of study area

mode system flown from a high-altitude aircraft. Figure 5 shows that the scene is rural and mountainous with sparse vegetation. The sporadic buildings are complex with indoor courtyards, multiple tiers, and perimeter walls. The data has very little noise and appears to have few outliers.

Site IV is in Mosul, Iraq (the section known as the Old City west of the Tigris). The site was surveyed by the Army Geospatial Centers BuckEye LiDAR system, which is a Geiger Mode system. Figure 6 shows that the scene contains a dense, urban area with complex structures and discontinuous terrain. The data has very little noise and few outliers.

## 2.5 Terrain Extraction Assessment

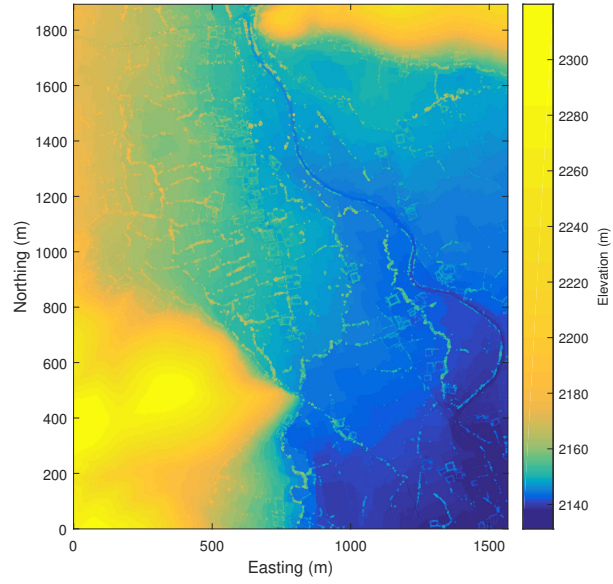
Algorithm performance was assessed following [2] by computing the Total Error, Type I Errors (bare-earth misclassified as object), and Type II Errors (objects misclassified as bare-earth). Errors were computed by comparing the MRF terrain/off-terrain classification map against the manually classified point cloud.

## 3 Results

To measure classification error, point clouds were manually classified point-by-point using the LP360 Standard software. All automated MRF classifications were performed at 1 m resolution. The point clouds were rasterized as the fifth percentile elevation in each grid cell. The fifth percentile was chosen to achieve a low elevation and avoid low blunders. Voids were filled by computing the Laplacian between non-void pixels.

The data energy and clique potential were balanced by setting  $\alpha = 0.75$  (which gives more weight to the data energy than the clique potential). The Gaussian half-width was set to  $\delta_0 = 1.5$  m (which is approximately half a building story). The radius of the averaging kernel (used to estimate  $z_{dtm}$  in Eq. 4&5) for each test dataset was adjusted to the features in the scenes (usually determined by the footprint of the largest building). Table 2 shows summary results.

**Site I** Figure 7c shows that Type I error mainly occurred at the terrain shelf in the southwest of the scene as well as along some of the residential streets that were lined with small trees. Type II errors occurred along perimeter



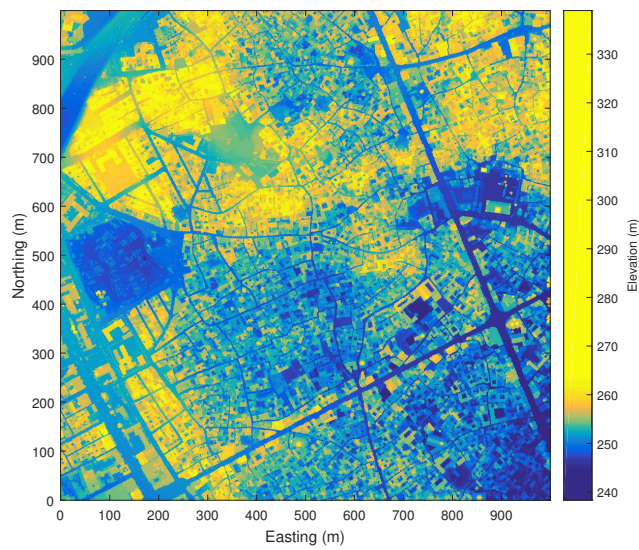
(a) DSM



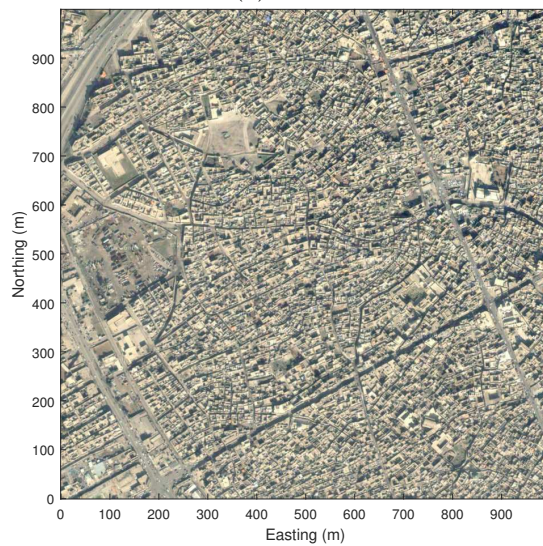
(b) Orthoimage

Figure 5: DSM from ALIRT LiDAR point cloud and orthoimage of study area





(a) DSM



(b) Orthoimage

Figure 6: DSM from BuckEye LiDAR point cloud and orthoimage of study area

	Site I	Site II	Site III	Site IV
Sensor	EO	Direct Mode	ALIRT	BuckEye
$\delta_0$ (m)	1.5	1.5	1.5	1.5
Radius (m)	50	20	10	35
Runtime (s)	25	9	93	71
Iterations	5	5	7	8
% Total Error	9	7	3	6
% Type I Error	7	1	3	3
% Type II Error	3	5	<1	3

Table 2: Parameters and summary results. The experiments were run on a Dell Precision M6700 laptop with 16 GB of RAM and an AMD 64 quad-core processor.

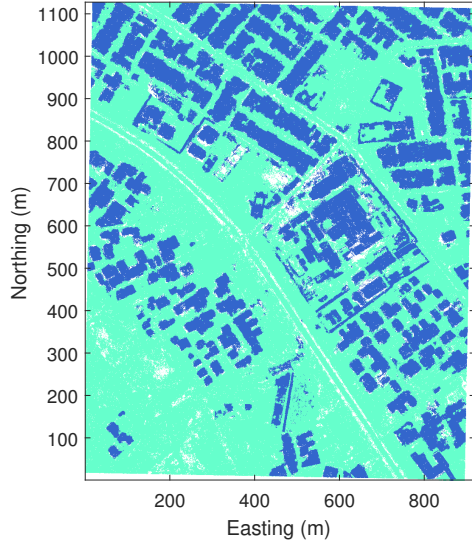
walls in along the hospital complex, which had a number of walls and low-relief buildings.

**Site II** Figure 8c shows that the classification errors were local and dispersed, and were not due to misclassification of entire land features or buildings. Site II had a greater prevalence of Type II Errors than Type I Errors, which is because suburban landscapes present small features (e.g., landscaping and fences). Small features that deviate from the terrain by less than  $\delta_0 = 1.5m$  are biased toward the terrain classification. Furthermore, the clique potential promotes class continuity, which can cause misclassification of fences or shrubs that are one or two pixels wide.

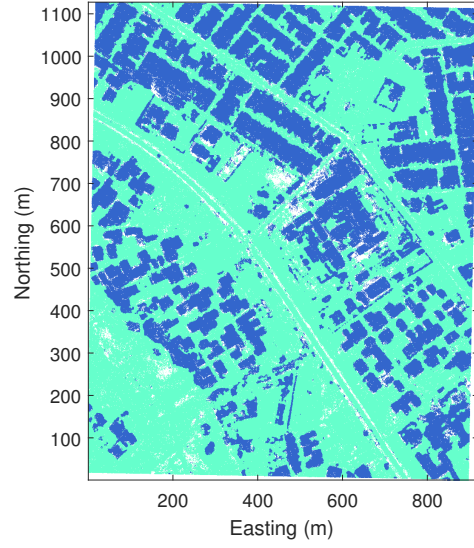
**Site III** Figure 9 shows that errors were not localized to one particular kind of feature. Some errors are clearly structures that were manually misclassified as terrain and correctly classified by the algorithm. Many of the localized errors in the southwest of the site were likely misclassified manually as earth and correctly classified as vegetation by the algorithm.

**Site IV** Figure 10 shows Type I errors in the northwest of the site due to terrain discontinuities where there is a sharp embankment next to the highway and retaining wall.

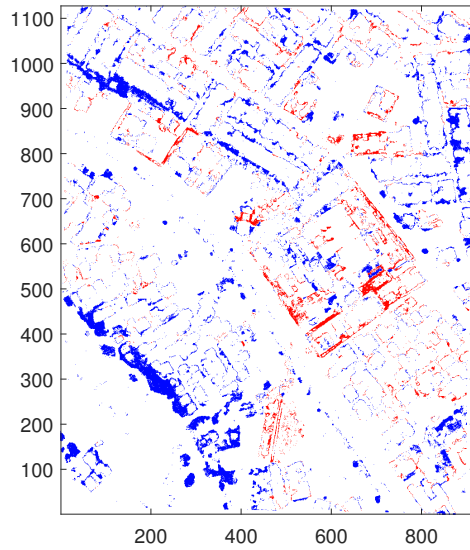




(a) Terrain/Off-terrain classifications from manual classification

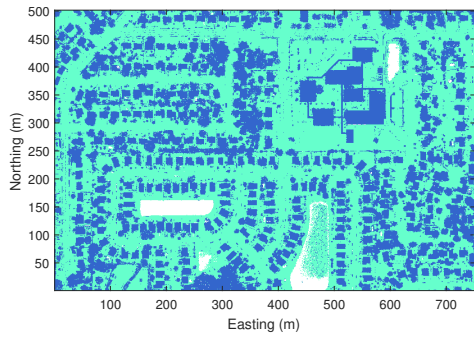


(b) Terrain/Off-terrain classifications from MRF algorithm

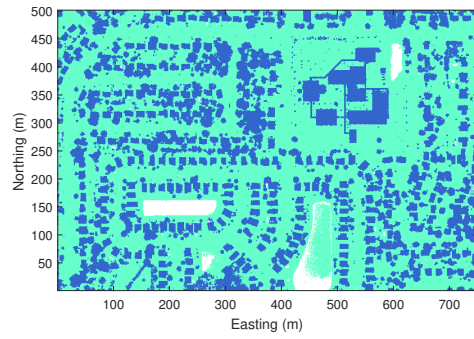


(c) Error map with Type I errors shown in blue and Type II errors shown in red

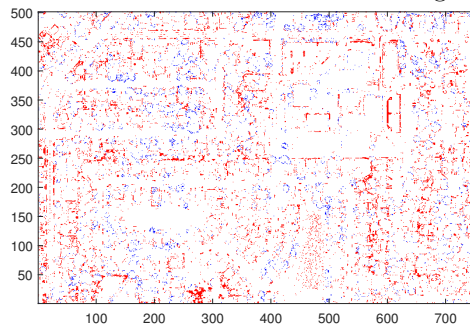
Figure 7: EO point cloud test results



(a) Terrain/Off-terrain classifications from manual classification

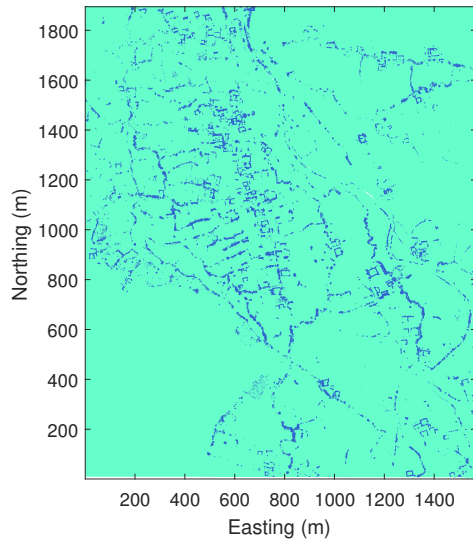


(b) Terrain/Off-terrain classifications from MRF algorithm

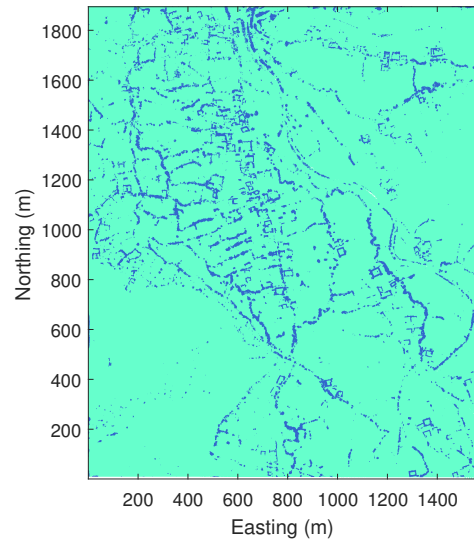


(c) Error map with Type I errors shown in blue and Type II errors shown in red

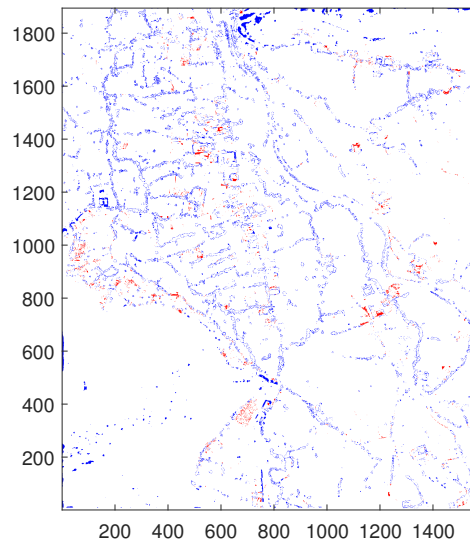
Figure 8: Direct Mode Lidar test results



(a) Terrain/Off-terrain classifications from manual classification



(b) Terrain/Off-terrain classifications from MRF algorithm



(c) Error map with Type I errors shown in blue and Type II errors shown in red

Figure 9: ALIRT point cloud test results

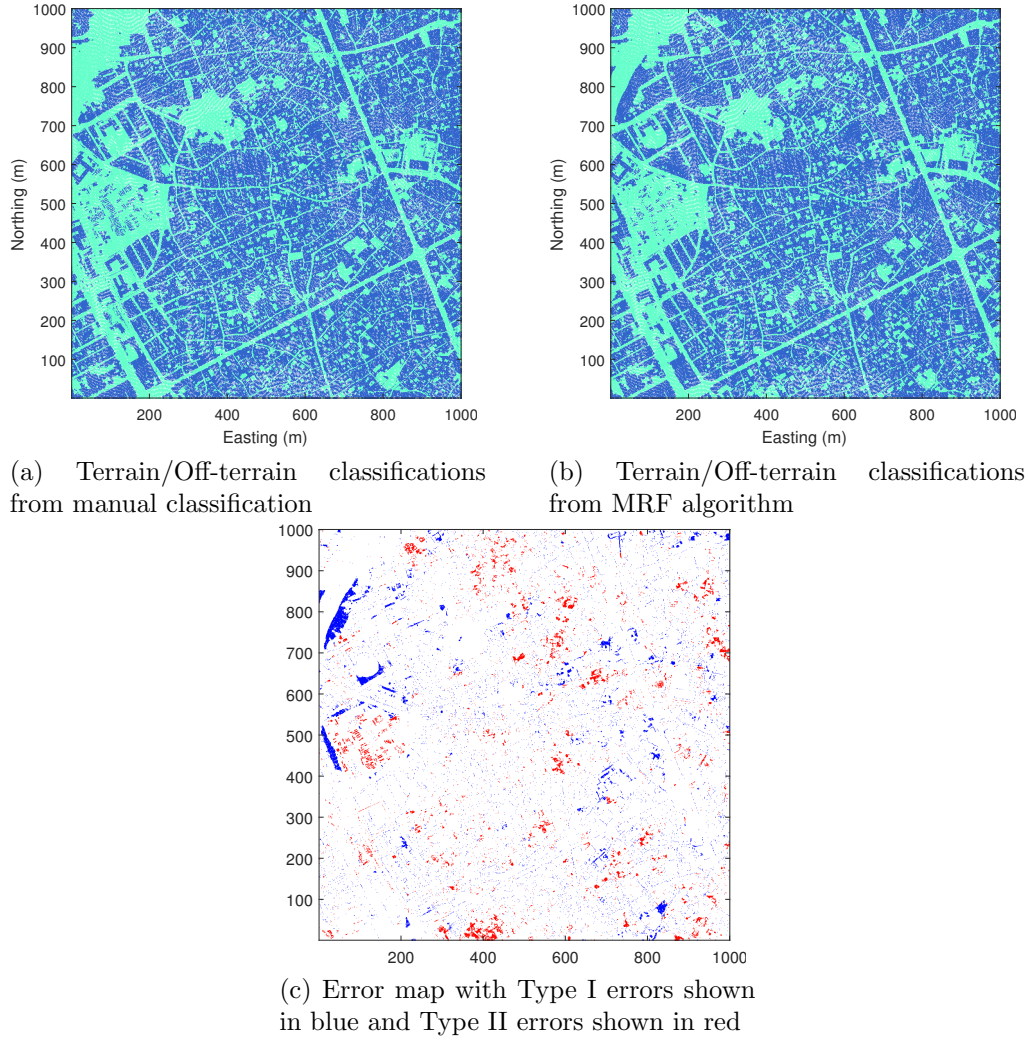


Figure 10: BuckEye Lidar test results

## 4 Discussion

### 4.1 Algorithm Strengths and Weaknesses

The low Total Error over the four tests suggests that the algorithm effectively segments terrain from off-terrain features. Low rates of Type II Errors indicates that the algorithm extracts high-confidence bare-earth areas, which is desirable for subsequent terrain reconstruction. The rates of Type I to Type II error can be tuned through the  $\delta_0$  and radius parameters.

The performance analysis indicated that the algorithm has trouble in scenes with large-footprint buildings and rapidly changing terrain. The error occurs because of the moving-average technique for estimating the DTM elevation. The radius of the averaging window needs to be large enough to capture enough terrain pixels to reliably estimate the elevation of the terrain. However, if the radius is too large, salient features in the terrain can be smoothed away causing small-scale hills or ledges to be misclassified as off-terrain. This trade-off is exemplified in Site I where the scene contains a large-footprint, low-relief hospital structure and a sharply-changing terrain shelf; the radius was set large enough to accurately classify the hospital but was too large to accurately represent all of the terrain.

A strength of the MRF energy formulation is that additional features can be incorporated in a natural way via new energy terms. That is, while elevation and EO spectra are incommensurable quantities, potentials that are functions of these quantities are themselves commensurable. [2] noted that none of the algorithms they evaluated made use of information in addition to elevation, and posed the use of additional information as a research issue for the community. Further, [17] noted that it is a strength of a bare earth algorithm that it provides a principled foundation that more complex criteria can be built upon.

Additionally, the algorithm is exceptionally easy to implement and contains a small number of intuitive parameters, namely smoothing radius (which is set by the width of the largest buildings) and  $\delta_0$  (which is set to about a half building story).

### 4.2 Future Work

We will soon extend the MRF model to incorporate point color or intensity, which is inherited from the source spectral and panchromatic imagery.

The additional intensity-based energy terms will encode an assumption that different features are typically perceptively different. Our intent is to improve accuracy where inference based on geometry alone is problematic, e.g., for a low-relief, large-footprint warehouse in which the roof is perceptively uniform and different from the ground around it, or for undulating terrain that is perceptively consistent. Incorporating perceptual attributes will mitigate the weakness of the moving-average technique by incorporating more evidence toward whether an area is bare-earth or an off-terrain object.

## 5 Conclusions

We have presented an MRF approach to terrain extraction from point clouds. We presented our energy potential formulations and justifications for those formulations. We improved upon the approach of [6] by applying graph cuts for exact and efficient energy minimization. We demonstrated that the algorithm effectively segments terrain from off-terrain features in an EO-derived point cloud, as well as in LiDAR point clouds collected from three different sensors. We also discussed the strengths and weaknesses of the algorithm, and future work.

## References

- [1] P. Musialski, P. Wonka, D. G. Aliaga, M. Wimmer, L. Gool, W. Purgathofer, A survey of urban reconstruction, in: Computer graphics forum, Vol. 32, Wiley Online Library, 2013, pp. 146–177.
- [2] G. Sithole, G. Vosselman, Experimental comparison of filter algorithms for bare-earth extraction from airborne laser scanning point clouds, ISPRS journal of photogrammetry and remote sensing 59 (1) (2004) 85–101.
- [3] N. Pfeifer, P. Stadler, C. Briese, Derivation of digital terrain models in the scop++ environment, in: Proceedings of OEEPE Workshop on Airborne Laserscanning and Interferometric SAR for Detailed Digital Terrain Models, Stockholm, Sweden, Vol. 3612, 2001.

- [4] M. Isenburg, J. Schewchuck, Lastools: converting, viewing, and compressing lidar data in las format, available at: <http://www.cs.unc.edu/~isenburg/lastools>.
- [5] C. Baillard, O. Dissard, O. Jamet, H. Maitre, Detection of above-ground in urban areas: application to dtm generation, *Image and Signal Processing for Remote Sensing III* 2955 (1996) 129–140.
- [6] C. Baillard, H. Maitre, 3-d reconstruction of urban scenes from aerial stereo imagery: a focusing strategy, *Computer Vision and Image Understanding* 76 (3) (1999) 244–258.
- [7] S. Geman, D. Geman, Stochastic relaxation, gibbs distributions, and the bayesian restoration of images, *IEEE Transactions on pattern analysis and machine intelligence* (6) (1984) 721–741.
- [8] D. Anguelov, B. Taskarf, V. Chatalbashev, D. Koller, D. Gupta, G. Heitz, A. Ng, Discriminative learning of markov random fields for segmentation of 3d scan data, in: 2005 IEEE Computer Society Conference on Computer Vision and Pattern Recognition (CVPR’05), Vol. 2, IEEE, 2005, pp. 169–176.
- [9] M. Häselich, M. Arends, D. Lang, D. Paulus, Terrain classification with markov random fields on fused camera and 3d laser range data., in: *ECMR*, 2011, pp. 153–158.
- [10] D. Ferrario, M. B. Cuadra, M. Schaer, N. Houhou, D. Zosso, S. Eliez, L. Guibaud, J.-P. Thiran, Brain surface segmentation of magnetic resonance images of the fetus, in: *Signal Processing Conference, 2008 16th European*, IEEE, 2008, pp. 1–5.
- [11] Z. Kato, T.-C. Pong, A markov random field image segmentation model for color textured images, *Image and Vision Computing* 24 (10) (2006) 1103–1114.
- [12] Z. Kato, J. Zerubia, M. Berthod, Satellite image classification using a modified metropolis dynamics, in: *Acoustics, Speech, and Signal Processing, 1992. ICASSP-92., 1992 IEEE International Conference on*, Vol. 3, IEEE, 1992, pp. 573–576.
- [13] C. M. Bishop, *Pattern recognition, Machine Learning* 128.

- [14] Y. Y. Boykov, M.-P. Jolly, Interactive graph cuts for optimal boundary & region segmentation of objects in nd images, in: Computer Vision, 2001. ICCV 2001. Proceedings. Eighth IEEE International Conference on, Vol. 1, IEEE, 2001, pp. 105–112.
- [15] D. M. Greig, B. T. Porteous, A. H. Seheult, Exact maximum a posteriori estimation for binary images, Journal of the Royal Statistical Society. Series B (Methodological) (1989) 271–279.
- [16] R. Knowlton, Airborne lidar imaging research testbed, Tech. rep., DTIC Document (2011).
- [17] T. J. Pingel, K. C. Clarke, W. A. McBride, An improved simple morphological filter for the terrain classification of airborne lidar data, ISPRS Journal of Photogrammetry and Remote Sensing 77 (2013) 21–30.